Chemical Science

ROYAL SOCIETY OF CHEMISTRY

EDGE ARTICLE

View Article Online
View Journal | View Issue

Cite this: *Chem. Sci.*, 2025, **16**, 7010

All publication charges for this article have been paid for by the Royal Society of Chemistry

Molecular engineering of 1D conjugated copper anilate coordination polymers for boosting electrocatalytic nitrate reduction to ammonia†

Zhanning Liu, ‡*[a] Chengyong Xing,‡[a] Yufei Shan,[a] Min Ma,[a] Shaowen Wu, [a] Ruixiang Ge,[b] Qingzhong Xue *[a] and Jian Tian *[a]

Received 17th December 2024
Accepted 17th March 2025

DOI: 10.1039/d4sc08508f

rsc.li/chemical-science

The electrochemical nitrate reduction reaction (NO_3RR) offers a "two-birds-one-stone" solution by simultaneously addressing water pollution and enabling green ammonia production. However, its multiple reaction pathways and complex intermediates pose a challenge for designing high-efficiency electrocatalysts. The highly modular nature of metal coordination polymers (MCPs), combined with molecular engineering strategies, provides a pathway for systematically exploring the structure–performance relationships of catalysts. As a proof of concept, we here synthesized a series of π–d conjugated copper anilate coordination polymers incorporating different halogen atoms (F, Cl and Br). The combined experimental and theoretical investigations reveal that introducing halogen atoms with electron-withdrawing properties can create an electron-deficient Cu center through the interchain Cu⋯halogen supramolecular interactions, which can effectively lower the energy barrier for deoxygenation of the *NO intermediate. As a result, the Cu–FA (FA = fluoranilate, $C_6O_4F_2^{2-}$) achieves a superior NO_3RR performance with the faradaic efficiency (FE) of 98.17% and yielding rate of 14.308 mg h^{-1} mg^{-1} at −0.9 V, nearly 7.7 times that of the pristine Cu–DABQ (DABQ = 2,5-dihydroxy-1,4-benzoquinone, $C_6O_4H_2^{2-}$). This study may provide new insights into the design of high-performance NO_3RR electrocatalysts.

Introduction

Ammonia (NH_3) synthesis has been one of the largest chemical industries since the early twentieth century, primarily due to its pivotal role in modern agriculture and industrial manufacturing.[1,2] Currently, ammonia is predominantly produced through the Haber–Bosch process, which not only demands high energy consumption but also results in significant carbon emission.[3] As such, there is an urgent need to develop more efficient alternative approaches, particularly those capable of functioning under ambient conditions. Electrocatalytic ammonia synthesis, which utilizes water as the proton source and renewable electrical energy, is emerging as a promising alternative.[4] Typically, the nitrogen source can be either nitrogen gas or various NO_x-based species.[5–7] Among them, nitrate stands out due to its relatively low dissociation energy and excellent water solubility,[8] both of which can significantly enhance reaction kinetics. Furthermore, as nitrate is a major pollutant in industrial and agricultural wastewater, the electrocatalytic nitrate reduction reaction (NO_3RR) offers the possibility of directly converting harmful NO_3^- into industrially valuable NH_3, thereby contributing to the management of the anthropogenic nitrogen cycle.[9–12] As a result, this process has recently attracted special attention.[13,14] Nevertheless, the electrochemical reduction of NO_3^- to NH_3 involves a complex eight electron-coupled nine proton transfer process, which tends to produce various intermediates and by-products.[15–17] Therefore, the atomic-level rational design of catalysts, particularly those based on earth-abundant metal ions, is crucial for the development of high-performance electrocatalysts.[18–23] Among the diverse reported electrocatalysts, copper-based complexes have been regarded as promising candidates owing to the notable alignment between the energy levels of the d-orbital on Cu and LUMO π* of NO_3^-.[15,22,23]

Metal coordination polymers (MCPs) or metal–organic frameworks (MOFs), a novel type of crystalline inorganic–organic hybrid materials, have been extensively investigated for applications in gas storage/separation,[24] heterogeneous catalysis,[25] sensing,[26] luminescence and so on.[27] The recently developed π–d conjugated MCPs, featuring excellent electronic conductivity, further sparked their potential in the

[a]*School of Materials Science and Engineering, Shandong University of Science and Technology, Qingdao, Shandong, 266590, P. R. China. E-mail: znliu@sdust.edu.cn; xueqz@upc.edu.cn; jiantian@sdust.edu.cn*

[b]*College of Chemical and Biological Engineering, Shandong University of Science and Technology, Qingdao, Shandong, 266590, P. R. China*

† Electronic supplementary information (ESI) available. See DOI: https://doi.org/10.1039/d4sc08508f

‡ Z. Liu and C. Xing contributed equally to this work.

electrochemical energy storage and conversion, including lithium/potassium batteries,[28,29] supercapacitors,[30] and electrocatalysis.[31] The unique delocalization of frontier π orbits of organic ligands and d orbits of transition metal ions can effectively mitigate the inherently low electronic conductivity of coordination bonds.[32] Moreover, the presence of well-defined open metal sites (OMS) and their highly modular local coordination environment can significantly deepen our understanding of structure–performance relationships.[5] Guided by molecular engineering strategies, some recent studies have demonstrated that careful ligand modification can effectively optimize the electronic structures of metal ions,[33–37] thereby significantly enhancing the electrocatalytic performance. For example, Chen *et al.* reported that altering the electron-withdrawing β-site substituents of Co-TAA (TAA = 1,4,8,11-tetraaza[14]annulene) can modulate the interactions between the intermediate species and active Co site, regulating the oxygen reduction reaction (ORR) performances.[35] More recently, Cheng *et al.* found that introducing polar functional groups (–NH_2 or –NO_2) on ZIF-7 can enhance the capture and activation of CO_2 during electrocatalytic CO_2 reduction.[36] Such findings underscore the critical role of ligand modification in tuning catalyst performance. Nevertheless, this approach has rarely been explored for the electrocatalytic NO_3RR.[37]

2,5-Dihydroxy-1,4-benzoquinone (H_2dhbq), also known as anilate ligand in its dianionic form (dhbq^{2-} or An^{2-}), has been extensively studied for its coordination polymers due to their intriguing magnetic and electronic properties.[38,39] Its remarkable chemical tolerance for halogen atoms (*e.g.*, F, Cl, Br) at the 3 and 6 positions (Scheme 1) makes the metal anilate complexes a perfect platform for exploring the influence of local environment on NO_3RR performance.[40] As a proof of concept, we herein synthesized a series of Cu–anilate based coordination polymers, named Cu–DHBQ, Cu–FA, Cu–CA, and Cu–BA, where FA, CA, and BA stand for fluoranilate ($C_6O_4F_2^{2-}$), chloranilate ($C_6O_4Cl_2^{2-}$) and bromoanilate ($C_6O_4Br_2^{2-}$), respectively, for clarity. It is found that the type of halogen atoms largely determines the NO_3RR performance. Stronger the electron-withdrawing ability, higher the NH_3 yield rate and faradaic efficiency (FE). Among them, Cu–FA achieves an exceptional NH_3 yield rate of 14.308 mg h^{-1} mg^{-1} with a FE of 98.17% at −0.9 V *vs.* Reversible Hydrogen Electrode (RHE), which is nearly 7.7 times that of the pristine Cu–DHBQ. Detailed structural characterization and theoretical calculations reveal that the introduction of halogen atoms can induce a positive shift in Cu valence, which can effectively lower the energy barrier, leading to the enhanced NO_3RR performance.

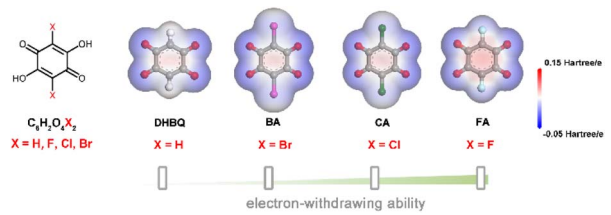

Scheme 1 Illustration of the molecular formula and electron-withdrawing ability of the anilate ligands.

Results and discussion

The Cu–anilate complexes were synthesized through a facile ultrasonic-standing method under ambient conditions.[41] In particular, an aqueous solution of copper(II) acetate was mixed with an aqueous solution of anilate ligand, followed by ultrasonic treatment for 2 min, and then left to stand for 12 h. Powder X-ray diffraction (PXRD) analysis was used to investigate the crystalline properties. As shown in Fig. S1,† Cu–DHBQ shows three broad diffraction peaks at 16.7°, 22.8° and 29.9°, inferring the low crystallinity. In contrast, Cu–FA, Cu–CA, and Cu–BA display sharp diffraction peaks, suggesting their highly crystalline nature. This enhanced crystallinity may be attributed to the presence of Cu···halogen interactions, which can effectively regulate the packing of coordination chains. The PXRD patterns of Cu–CA and Cu–BA closely align with the previously reported structure,[42] confirming that they share an identical 1D chain structure (Fig. 1a and b). A noticeable peak shift can be identified for Cu–FA compared to Cu–CA, which may originate from the subtle variations in interchain packing and orientation. Besides, scanning electron microscopy (SEM) and transmission electron microscopy (TEM) images showed that Cu–FA, Cu–CA and Cu–BA possess much more regular morphology than Cu–DHBQ (Fig. 1c, d and S2–S4†). Energy-dispersive X-ray spectroscopy (EDS) mapping analyses confirm the presence of Cu, O, C, X (X = F, Cl, Br for Cu–FA, Cu–CA, and Cu–BA, respectively) and demonstrate their homogeneous distribution throughout the particles (Fig. 1e and S2–S4†). Notably, the as-synthesized Cu–FA showed a prismatic morphology (Fig. 1c). Following extensive ultrasonic treatment, it fractured into thin needles (Fig. 1d), further indicating its 1D coordination crystal structure.

High-resolution X-ray photoelectron spectroscopy (XPS) measurements were conducted to gain insights into the chemical states of Cu ions. For Cu–FA (Fig. 2a), the peaks at 935.8 and 955.5 eV are attributed to Cu $2p_{3/2}$ and $2p_{1/2}$,[42] respectively, while the other species are satellite peaks, revealing the chemical state of Cu^{2+}. The other three compounds exhibit similar XPS peaks, indicating a comparable oxidation state. A detailed

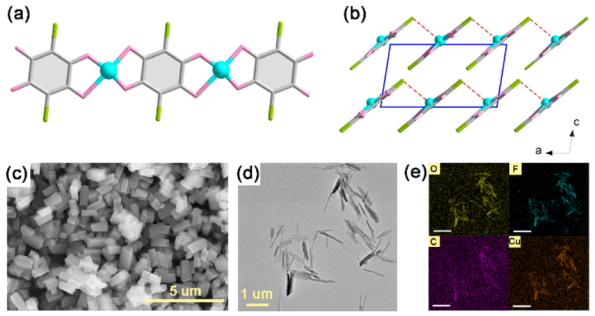

Fig. 1 Illustration of the coordination chain (a) and interchain packing of copper anilate complexes (b). SEM (c), TEM (d) and the corresponding elemental mappings manifest the images (e) of Cu–FA.

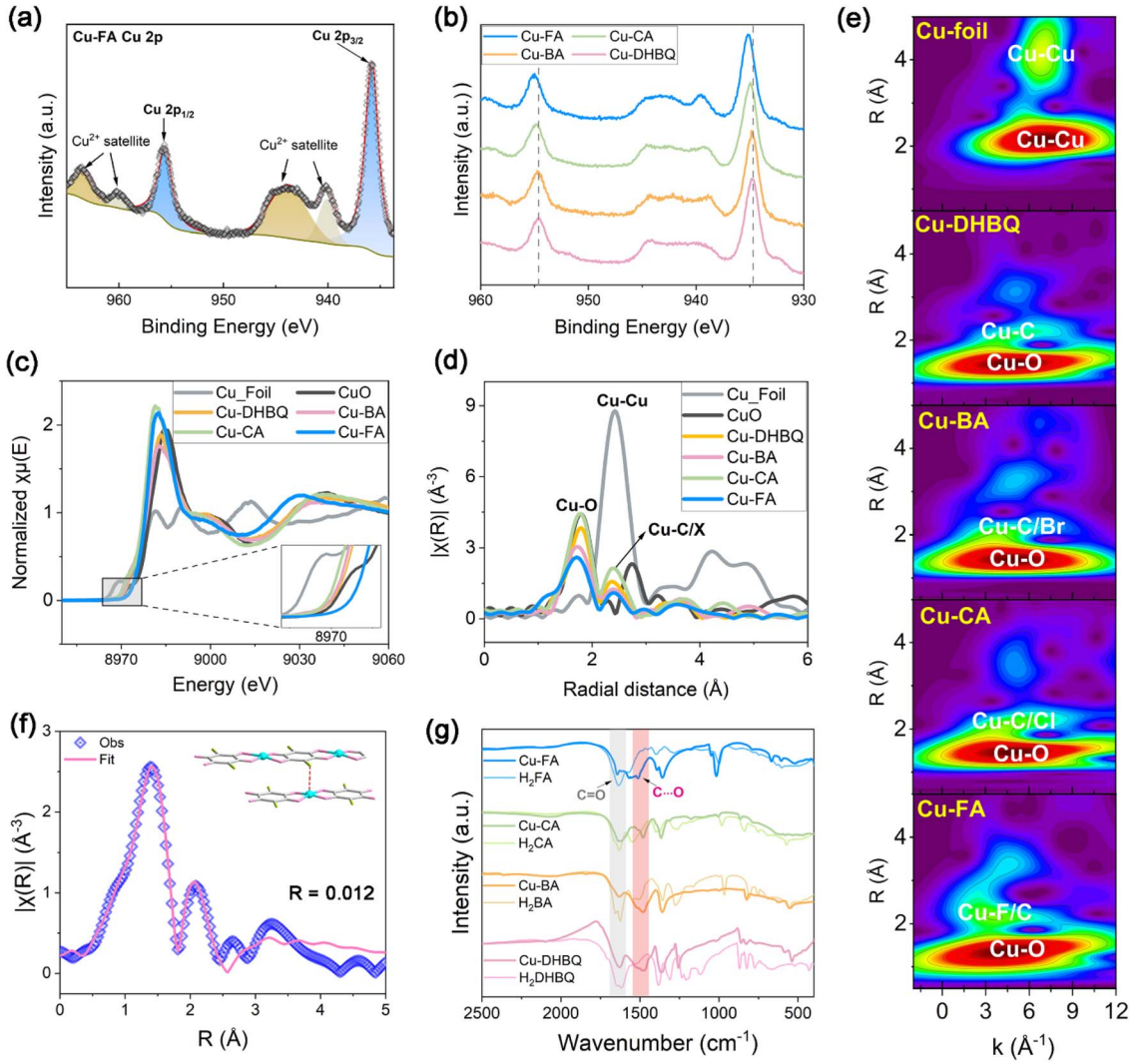

Fig. 2 (a) High-resolution XPS spectra of Cu 2p of Cu–FA and corresponding peak identification. (b) Peak shift comparison of Cu 2p XPS spectra of Cu–FA, Cu–CA, Cu–BA, and Cu–DHBQ. Cu K-edge XANES (c), EXAFS (d) spectra and the corresponding wavelet transforms (e) for different samples. (f) Fitted EXAFS cure ($R = 0.012$) and the inset illustrates the structural model. (g) FT-IR spectra of the synthesized Cu anilate complexes (bold dark line) and their corresponding anilic acids (narrow light line).

comparison revealed that halogen substitution on the anilate ligand results in a positive shift in the binding energies for Cu^{2+} (Fig. 2b). In particular, for Cu–FA, the binding energy shifts by ~0.4 eV compared to the pristine Cu–DHBQ, indicating an increased oxidation state of Cu. This shift may be attributed to the strong electron-withdrawing effect of the F atom from the adjacent chain. To further investigate the electron structures and local coordination structures of these samples, X-ray adsorption fine structure (XAFS) data at the Cu K-edge were collected. As shown in Fig. 2c, the adsorption edges of the four samples closely resemble that of CuO, confirming the Cu^{2+} oxidation state. Among them, Cu–FA shows a noticeable positive shift compared to the others, implying the increased oxidation state of Cu, which is in accordance with the XPS result. Additionally, the absence of a distinct pre-edge peak (1s–3d transition) in the four Cu–anilate complexes suggests that they possess similar square-planar coordination environments.[43,44] This was further supported by the extended X-ray adsorption fine structure (EXAFS) analyses. As shown in Fig. 2d, all the four samples show two-well resolved peaks due to the first and second coordination spheres. The first peak at ~1.78 Å is attributed to the Cu–O bond, while the second coordination shell peak at ~2.39 Å is assigned to the Cu–C/X (X = F, Cl Br) pairs. It should be noted that although the second peak may appear close to the Cu–Cu pairs (2.41 Å) in Cu-foil, the wavelet transform (WT) contour plot shows a dramatic difference in the *k*-space (Fig. 2e). The lobe corresponding to Cu–Cu pairs is mainly located at ~7.1 $Å^{-1}$, whereas the Cu–C/X pairs are found in the range 3.5–4.5 $Å^{-1}$, thereby ruling out the possibility of Cu nanoparticle formation. Moreover, the lobe corresponding to the Cu–C/F pairs shows a noticeable shift toward lower *k*-values compared to the other compounds, likely due to the lower atomic weight of F, further confirming the presence of Cu···F interactions.[45] The EXAFS curve of Cu–FA fits

well with the proposed chain structural model (Fig. 2f and Table S1†), validating the accuracy of this structure. The fitted EXAFS spectrum is not phase-corrected, so a shift with respect to the actual pair distances can be identified. Fourier-transform infrared (FT-IR) spectra were recorded to examine the changes of the ligand before and after coordination. Compared to the corresponding pristine anilic acids (Fig. 2g), the C=O vibrations at 1626–1655 cm^{-1} are noticeably weakened, while new peaks corresponding to C–O vibrations emerge in the range 1482–1516 cm^{-1} for the Cu–anilate complexes. This change is attributed to the electron delocalization between C=O and C–O, confirming that all four oxygen atoms participate in coordination.[46] Therefore, the results of PXRD, XPS, XAFS and FT-IR spectra provide solid evidence for the square planar Cu–O_4 coordination structure and the electron-deficient state of Cu centers following the substitution of halogen atoms.

Electrocatalytic NO_3RR performance of these compounds was then evaluated in a three-electrode H-cell setup containing 0.1 M Na_2SO_4 and 0.1 M KNO_3. Fig. 3a shows the linear sweep voltammetry (LSV) curves with or without NO_3^-. Evidently, all samples exhibit enhanced current in the presence of NO_3^-, indicating their electrocatalytic NO_3RR activity. By comparison, the current density of these compounds follows the trend Cu–FA > Cu–CA > Cu–BA > Cu–DHBQ, aligning with the electron-withdrawing ability of substituted halogen (or H) atoms. Based on the LSV result, a series of NO_3RR measurements were conducted at different potentials ranging from −0.5 to −1.0 V *vs.* RHE, and the corresponding chronoamperometry curves are shown in Fig. S5.† The generated products were quantitively determined using colorimetric methods with ultraviolet-visible (UV-vis) spectroscopy (Fig. S6†). Across all samples, nitrite (NO_2^-) and NH_3 were identified as the primary liquid-phase products, while no detectable hydroxylamine was observed (Fig. S7†).[14,17,47] At −0.5 V *vs.* RHE, NO_2^- formation was detected with the FE of ~2.60%, ~11.96%, ~43% and ~13.86% for Cu–FA, Cu–CA, Cu–BA, and Cu–DHBQ, respectively. As the applied potential became more negative, the FE associated with NO_2^- generation gradually decreased for all samples, likely due to

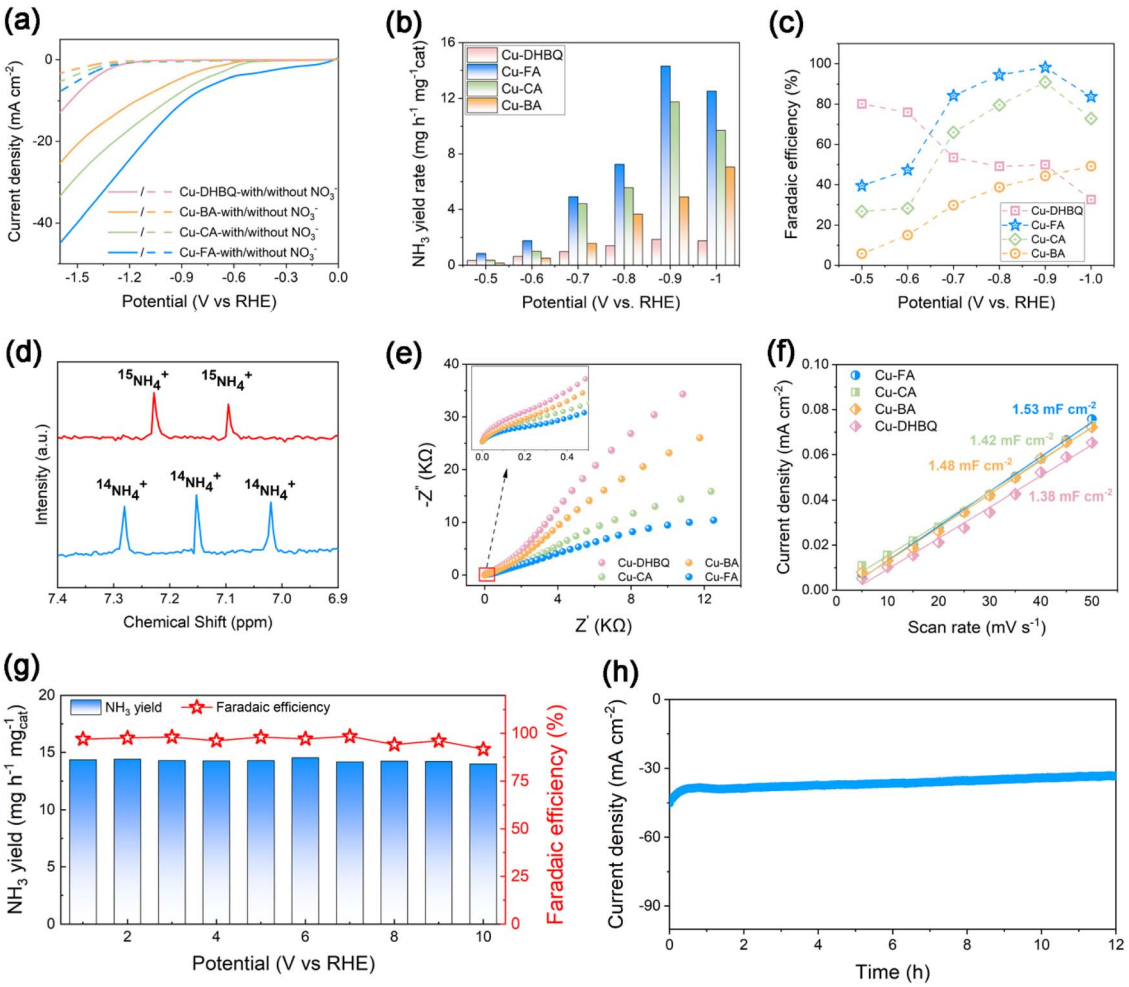

Fig. 3 (a) LSV curves in the electrolyte with (solid line) and without (dashed line) NO_3^- for Cu–DHBQ (pink), Cu–BA (orange), Cu–CA (green), and Cu–FA (blue). The NH_3 yield rate (b) and corresponding FE (c) at different potentials for different materials. (d) ^{1}H NMR spectra of the products after the NO_3RR of Cu–FA using $K^{14}NO_3$ and $K^{15}NO_3$ as the feeding nitrogen sources. EIS (e) and ECSA (f) of different samples. (g) Time-dependent long-term current density cure at −0.9 V (*vs.* RHE) for the duration of 12 h. (h) The cycling stability tests of Cu–FA at −0.9 V (*vs.* RHE) for 10 cycles.

enhanced deoxygenation and hydrogenation processes, as well as the increasing contribution of the competitive hydrogen evolution reaction (Fig. S8†). Notably, at −0.9 V *vs.* RHE, Cu–FA delivers the highest selectivity for NH_3 production, achieving an impressive FE of 98.17% with a yield rate of 14.308 mg h^{-1} mg^{-1}. This performance surpasses most of the reported electrocatalysts (Table S2†). In contrast, the highest NH_3 yield rates for Cu–DHBQ, Cu–CA and Cu–BA are only 1.851 mg h^{-1} mg^{-1}, 11.753 mg h^{-1} mg^{-1} and 7.048 mg h^{-1} mg^{-1}, respectively, with the FE of 49.88%, 90.95 and 49.12%. To validate the origin of ammonia production, a ^{15}N isotope labelling experiment was conducted. As depicted in Fig. 3d, the ^1H nuclear magnetic resonance (NMR) spectra using $^{15}NO_3^-$ as the feeding nitrogen source displays the characteristic doublet of $^{15}NH_4^+$ with a coupling constant of 72 Hz, whereas the use of $^{14}NO_3^-$ results in the detection of $^{14}NH_4^+$ with a triplet coupling peak. This confirms that the NH_3 detected in the electrolyte originates from nitrate reduction rather than atmospheric nitrogen contamination. Electrochemical impedance spectroscopy (EIS) measurements were performed to characterize the conductivity of electrodes (Fig. 3e). Among them, Cu–FA exhibits the lowest interfacial electron transfer resistance value, suggesting its superior electrocatalytic kinetics. Meanwhile, the electrochemically active surface area (ECSA) measurements (Fig. 3f and S9†) demonstrate that these four samples possess comparable ECSAs for NO_3^- reduction, ranging from 1.38 to 1.53 mF cm^{-2}. Thus, the impressive NO_3RR performance of Cu–FA is likely due to its intrinsic catalytic activity. The durability of Cu–FA in the NO_3RR was assessed through ten consecutive electrolysis cycles at −0.9 V. Following these ten cycles, no significant decline in NH_3 yield rate or FE can be observed (Fig. 3g). Additionally, the cathodic current in the time–current profile over 12 h shows negligible decay (Fig. 3h), further confirming its long-term stability and promising potential for practical applications.

The reaction kinetics and pathways were then investigated to gain insights into the mechanism underlying the enhanced NO_3RR performance of Cu–FA. *In situ* attenuated total reflectance Fourier transform infrared (ATR-FTIR) spectroscopy was employed to probe the possible reaction intermediates and pathways. As depicted in Fig. 4a and b, the peak intensities are potential dependent from OCP to −1.0 V. Among them, the peaks at 1375 cm^{-1} and 1445 cm^{-1} correspond to the adsorbed NO_3^- and NH_3,[7,48] while the peaks at 1514 cm^{-1}, 1256 cm^{-1} and 1188 cm^{-1} represent the formed *NO, *NH_2 and *NO_2 intermediates, respectively.[16,49] These characteristic peaks suggest that the electrocatalytic NO_3RR might follow a successive deoxygenation and hydrogenation process. Noticeably, a distinct band at ~1326 cm^{-1}, attributed to the symmetric stretching vibration of *NO_2,[50,51] can be clearly observed in the spectra of Cu–BA, whereas it is barely detectable for Cu–FA. This observation is consistent with the detected NO_2^- by-product and lower electrochemical NO_3RR FE observed for Cu–BA. Subsequently, density functional theory (DFT) calculations were carried out. The partial density of states (PDOS) for these compounds are plotted in Fig. S10.† A strong orbital hybridization between O 2p and Cu 3d orbitals can be identified, which is consistent with the π–d conjugation and large electron delocalization along the chain.

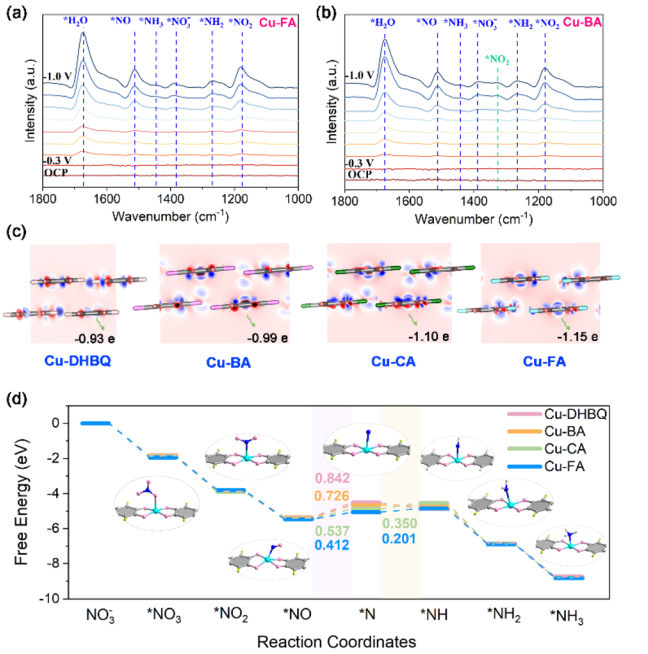

Fig. 4 (a) *In situ* ATR-FTIR spectra of Cu–FA (a) and Cu–BA (b) during the NO_3RR at different potentials (−0.3–−1.0 V). (c) Structural model and the charge difference viewing perpendicular to the chain packing direction. (d) Calculated Gibbs free energy diagram along the catalytic reaction pathway on different catalysts. The insets illustrate the adsorption configurations of various reaction intermediates.

The different charge distribution diagrams are shown in Fig. 4c, where the charge density distribution around halogen atoms is notably elongated in the chain packing direction, suggesting electron transfer between Cu and halogen atoms. Further Bader charge analysis revealed Cu charges of 0.93, 0.99, 1.10, and 1.15 in Cu–DHBQ, Cu–BA, Cu–CA and Cu–FA, respectively. This indicates that the introduction of halogen atoms shifts the Cu center from an electron-rich state to an electron-deficient state, aligning with the experimental XPS and XANES results. The electron-deficient state is believed to be beneficial for the adsorption of NO_3^- and nucleophilic intermediates,[19,37,52] and thus is expected to enhance the reaction performance. The Gibbs free energy was then analysed to investigate the reaction mechanism (Fig. 4d). The results indicate that the major potential-determining step (PDS) over these catalysts is the deoxygenation of *NO. In particular, the energy barrier of this PDS decreases progressively from Cu–DHBQ (ΔG = 0.842 eV) to Cu–BA (ΔG = 0.726 eV), Cu–CA (ΔG = 0.537 eV), and Cu–FA (ΔG = 0.412 eV), which is in agreement with the experimentally observed ammonia production performance. All these DFT results theoretically support the notion that introducing electron-withdrawing groups can effectively regulate the electronic structure of the active center, leading to enhanced electrocatalytic NO_3RR performance.

Conclusions

In summary, four π–d conjugated copper anilate coordination polymers were successfully synthesized. Their well-defined atomic structures provide insight into the underlying

mechanism of the NO_3RR. The electrocatalytic performance follows the trend Cu–FA > Cu–CA > Cu–BA > Cu–DHBQ, which is consistent with the electron-withdrawing capabilities of the substituted halogen atoms. Remarkably, Cu–FA exhibits an exceptional NH_3 yield rate of 14.308 mg h^{-1} mg^{-1} and a faradaic efficiency (FE) of 98.17% at −0.9 V (*vs.* RHE). The combination of XPS, XAFS, *in situ* FT-IR and DFT calculations reveal that the introduction of halogen atoms can produce an electron-deficient active center, which can facilitate the adsorption of intermediate *N and lower the energy barrier of the PDS, thereby enhancing NO_3RR performance. This design concept of using electron-withdrawing groups to tailor the electronic structure may pave the way for the development of high-efficiency NO_3RR and related electrocatalysts.

Data availability

The data supporting this article have been included as part of the ESI.†

Author contributions

Conceptualization, Zhanning Liu; methodology and investigation, Zhanning Liu, Chengyong Xing, and Yufei Shan; software, Ruixiang Ge and Qingzhong Xue; formula analysis, Min Ma and Shaowen Wu; writing – review and editing, Zhanning Liu and Jian Tian; funding acquisition, Zhanning Liu; resources, Qingzhong Xue and Jian Tian. All authors have read and agreed to the published version of the manuscript.

Conflicts of interest

There are no conflicts to declare.

Acknowledgements

This work was supported by the National Natural Science Foundation of China (Grant No. 22005340), Qingdao Natural Science Foundation (24-4-4-zrjj-194-jch) and Natural Science Foundation of Shandong Province (No. ZR2023QB215).

Notes and references

1 D. R. MacFarlane, P. V. Cherepanov, J. Choi, B. H. Suryanto, R. Y. Hodgetts, J. M. Bakker, F. M. F. Vallana and A. N. Simonov, A roadmap to the ammonia economy, *Joule*, 2020, **4**, 1186–1205.

2 K. Zhang, A. Cao, L. H. Wandall, J. Vernieres, J. Kibsgaard, J. K. Nørskov and I. Chorkendorff, Spin-mediated promotion of Co catalysts for ammonia synthesis, *Science*, 2024, **383**, 1357–1363.

3 C. Smith, A. K. Hill and L. Torrente-Murciano, Current and future role of Haber–Bosch ammonia in a carbon-free energy landscape, *Energy Environ. Sci.*, 2020, **13**, 331–344.

4 S. Li, X. Fu, J. K. Nørskov and I. Chorkendorff, Towards sustainable metal-mediated ammonia electrosynthesis, *Nat. Energy*, 2024, 1–6.

5 C. Xing, J. Ren, L. Fan, J. Zhang, M. Ma, S. Wu, Z. Liu and J. Tian, π-d conjugated copper chloranilate with distorted $Cu\text{-}O_4$ site for efficient electrocatalytic ammonia production, *Adv. Funct. Mater.*, 2024, 2409064.

6 Z. Wang, X. Wang, M. Yun, X. Shi, X. Xiao, Y. Liu, F. Yang, Y. Jiang and Y. Chen, Polyethyleneimine modified Au core Rh shell nanodendrites for light-promoted nitrite reduction reaction at low concentration, *J. Energy Chem.*, 2025, **103**, 400–407.

7 S. Xu, D. C. Ashley, H.-Y. Kwon, G. R. Ware, C.-H. Chen, Y. Losovyj, X. Gao, E. Jakubikova and J. M. Smith, A flexible, redox-active macrocycle enables the electrocatalytic reduction of nitrate to ammonia by a cobalt complex, *Chem. Sci.*, 2018, **9**, 4950–4958.

8 H. Zhang, H. Wang, X. Cao, M. Chen, Y. Liu, Y. Zhou, M. Huang, L. Xia, Y. Wang and T. Li, Unveiling cutting-edge developments in electrocatalytic nitrate-to-ammonia conversion, *Adv. Mater.*, 2024, **36**, 2312746.

9 P. H. van Langevelde, I. Katsounaros and M. T. Koper, Electrocatalytic nitrate reduction for sustainable ammonia production, *Joule*, 2021, **5**, 290–294.

10 H. Xu, Y. Ma, J. Chen, W.-x. Zhang and J. Yang, Electrocatalytic reduction of nitrate-a step towards a sustainable nitrogen cycle, *Chem. Soc. Rev.*, 2022, **51**, 2710–2758.

11 Q. Hong, B. Miao, T. Wang, F. Li and Y. Chen, Intermetallic PtTe metallene for formic acid oxidation assisted electrocatalytic nitrate reduction, *Energy Lab*, 2023, **1**, 220022.

12 K. Wang, R. Mao, R. Liu, J. Zhang, H. Zhao, W. Ran and X. Zhao, Intentional corrosion-induced reconstruction of defective NiFe layered double hydroxide boosts electrocatalytic nitrate reduction to ammonia, *Nat. Water.*, 2023, **1**, 1068–1078.

13 Y. Hu, J. Liu, W. Luo, J. Dong, C. Lee, N. Zhang, M. Chen, Y. Xu, D. Wu, M. Zhang, Q. Zhu, E. Hu, D. Geng, L. Zhong and Q. Yan, Alloying Pd with Ru enables electroreduction of nitrate to ammonia with ∼100% faradic efficiency over a wide potential window, *Chem. Sci.*, 2024, **15**, 8204–8215.

14 Z. Wu, M. Karamad, X. Yong, Q. Huang, D. A. Cullen, P. Zhu, C. Xia, Q. Xiao, M. Shakouri, F. Chen, J. Y. Kim, Y. Xia, K. Heck, Y. Hu, M. S. Wong, Q. Li, I. Gates, S. Siahrostami and H. Wang, Electrochemical ammonia synthesis via nitrate reduction on Fe single atom catalyst, *Nat. Commun.*, 2021, **12**, 2870.

15 G.-F. Chen, Y. Yuan, H. Jiang, S. Y. Ren, L. X. Ding, L. Ma, T. Wu, J. Lu and H. Wang, Electrochemical reduction of nitrate to ammonia via direct eight-electron transfer using a copper-molecular solid catalyst, *Nat. Energy*, 2020, **5**, 605–613.

16 O. Q. Carvalho, R. Marks, H. K. K. Nguyen, M. E. Vitale-Sullivan, S. C. Martinez, L. Arnadottir and K. A. Stoerzinger, Role of electronic structure on nitrate reduction to ammonium: a periodic journey, *J. Am. Chem. Soc.*, 2022, **144**, 14809–14818.

17 H. Li, J. Park, Y. Chen, Y. Qiu, Y. Cheng, K. Srivastava, S. Gu, B. H. Shanks, L. T. Roling and W. Li, Electrocatalytic nitrate

reduction on oxide-derived silver with tunable selectivity to nitrite and ammonia, *ACS Catal.*, 2021, **11**, 8431–8442.

18 M. Wang, S. Li, Y. Gu, W. Xu, H. Wang, J. Sun, S. Chen, Z. Tie, J. L. Zuo and J. Ma, Polynuclear cobalt cluster-based coordination polymers for efficient nitrate-to-ammonia electroreduction, *J. Am. Chem. Soc.*, 2024, **146**, 20439–20448.

19 A. Kumar, J. Lee, M. G. Kim, B. Debnath, X. Liu, Y. Hwang, Y. Wang, X. Shao, A. R. Jadhav and Y. Liu, Efficient nitrate conversion to ammonia on f-block single-atom/metal oxide heterostructure via local electron-deficiency modulation, *ACS Nano*, 2022, **16**, 15297–15309.

20 Y. Lv, S. Ke, Y. Gu, B. Tian, L. Tang, P. Ran, Y. Zhao, J. Ma, J. Zuo and M. Ding, Highly efficient electrochemical nitrate reduction to ammonia in strong acid conditions with Fe_2M-trinuclear-cluster metal-organic frameworks, *Angew. Chem., Int. Ed.*, 2023, **62**, e202305246.

21 J. Miao, Q. Hong, L. Liang, G. Li, Z. Liu, S. Yin and Y. Chen, B and Fe co-doped Co_2P hollow nanocubes for nitrate electroreduction to ammonia, *Chin. Chem. Lett.*, 2024, **35**, 108935.

22 W. Wang, J. Chen and E. C. M. Tse, Synergy between Cu and Co in a layered double hydroxide enables close to 100% nitrate-to-ammonia selectivity, *J. Am. Chem. Soc.*, 2023, **145**, 26678–26687.

23 W. He, J. Zhang, S. Dieckhofer, S. Varhade, A. C. Brix, A. Lielpetere, S. Seisel, J. R. C. Junqueira and W. Schuhmann, Splicing the active phases of copper/cobalt-based catalysts achieves high-rate tandem electroreduction of nitrate to ammonia, *Nat. Commun.*, 2022, **13**, 1129.

24 A. E. Amooghin, H. Sanaeepur, R. Luque, H. Garcia and B. Chen, Fluorinated metal-organic frameworks for gas separation, *Chem. Soc. Rev.*, 2022, **51**, 7427–7508.

25 W. Han, J. Li, R. Zhu, M. Wei, S. Xia, J. Fu, J. Zhang, H. Pang, M. Li and Z. Gu, Photosensitizing metal covalent organic framework with fast charge transfer dynamics for efficient CO_2 photoreduction, *Chem. Sci.*, 2024, **15**, 8422–8429.

26 X. C. Zhou, C. Liu, J. Su, Y. F. Liu, Z. Mu, Y. Sun, Z. M. Yang, S. Yuan, M. Ding and J. L. Zuo, Redox-active mixed-linker metal-organic frameworks with switchable semiconductive characteristics for tailorable chemiresistive sensing, *Angew. Chem., Int. Ed.*, 2023, **62**, e202211850.

27 P.-Y. Fu, S.-Z. Yi, M. Pan and C. Y. Su, Excited-state intramolecular proton transfer (ESIPT) based metal-organic supramolecular optical materials: Energy transfer mechanism and luminescence regulation strategy, *Acc. Mater. Res.*, 2023, **4**, 939–952.

28 J. Geng, Y. Ni, Z. Zhu, Q. Wu, S. Gao, W. Hua, S. Indris, J. Chen and F. Li, Reversible metal and ligand redox chemistry in two-dimensional iron-organic framework for sustainable lithium-Ion batteries, *J. Am. Chem. Soc.*, 2023, **145**, 1564–1571.

29 J. Wang, H. Jia, Z. Liu, J. Yu, L. Cheng, H. G. Wang, F. Cui and G. Zhu, Anchoring π-d conjugated metal-organic frameworks with dual-active centers on carbon nanotubes for advanced potassium-ion batteries, *Adv. Mater.*, 2024, **36**, 2305605.

30 S. Shang, C. Du, Y. Liu, M. Liu, X. Wang, W. Gao, Y. Zou, J. Dong, Y. Liu and J. Chen, A one-dimensional conductive metal-organic framework with extended π-d conjugated nanoribbon layers, *Nat. Commun.*, 2022, **13**, 7599.

31 D. Huang, X. Qiu, J. Huang, M. Mao, L. Liu, Y. Han, Z. Zhao, P. Liao and X. Chen, Electrosynthesis of urea by using Fe2O3 nanoparticles encapsulated in a conductive metal–organic framework, *Nat. Synth.*, 2024, **3**, 1404–1413.

32 L. S. Xie, G. Skorupskii and M. Dinca, Electrically conductive metal–organic frameworks, *Chem. Rev.*, 2020, **120**, 8536–8580.

33 Y. Liu, X. Li, S. Zhang, Z. Wang, Q. Wang, Y. He, W. H. Huang, Q. Sun, X. Zhong and J. Hu, Molecular engineering of metal-organic frameworks as efficient electrochemical catalysts for water oxidation, *Adv. Mater.*, 2023, **35**, 2300945.

34 T. A. Al-Attas, N. N. Marei, X. Yong, N. G. Yasri, V. Thangadurai, G. Shimizu, S. Siahrostami and M. G. Kibria, Ligand-engineered metal–organic frameworks for electrochemical reduction of carbon dioxide to carbon monoxide, *ACS Catal.*, 2021, **11**, 7350–7357.

35 B. Huang, X. Tang, Y. Hong, L. Li, T. Hu, K. Yuan and Y. Chen, Electron-donors-acceptors interaction enhancing electrocatalytic activity of metal-organic polymers for oxygen reduction, *Angew. Chem., Int. Ed.*, 2023, **135**, e202306667.

36 X. Zhang, J. Chen, G. Wang, Y. Dong, J. Ji, L. Li, M. Xue and H. M. Cheng, Controlling the polarity of metal-organic frameworks to promote electrochemical CO_2 reduction, *Angew. Chem., Int. Ed.*, 2024, e202416367.

37 R. Zhang, H. Hong, X. Liu, S. Zhang, C. Li, H. Cui, Y. Wang, J. Liu, Y. Hou and P. Li, Molecular engineering of a metal-organic polymer for enhanced electrochemical nitrate-to-ammonia conversion and zinc nitrate batteries, *Angew. Chem., Int. Ed.*, 2023, **62**, e202309930.

38 X. Gao, Y. Wang, L. T. Menezes, Z. Huang, H. Kleinke and Y. Li, Stable 2,5-Dihydroxy-1,4-benzoquinone Based Organic Cathode Enabled by Coordination Polymer Formation and Binder Optimization, *Adv. Funct. Mater.*, 2024, **34**, 2315669.

39 M. E. Ziebel, C. A. Gaggioli, A. B. Turkiewicz, W. Ryu, L. Gagliardi and J. R. Long, Effects of covalency on anionic redox chemistry in semiquinoid-based metal-organic frameworks, *J. Am. Chem. Soc.*, 2020, **142**, 2653–2664.

40 Y. Lu, Y.-X. Deng, Y.-J. Lin, Y.-F. Han, L.-H. Weng, Z.-H. Li and G.-X. Jin, Molecular borromean rings based on dihalogenated ligands, *Chem*, 2017, **3**, 110–121.

41 Z. Liu, Q. Li, Y. Wang, R. Ma, J. Sun, J. Deng, J. Chen, D. Sun and X. Xing, Facile synthesis of dicelike cobalt squarate cages through a spontaneous dissolution–regrowth process, *Chem. Mater.*, 2020, **32**, 6765–6771.

42 Y. Luo, J. Liu and L. Zhang, A monocrystalline coordination polymer with multiple redox centers as a high-performance cathode for lithium-ion batteries, *Angew. Chem., Int. Ed.*, 2022, **134**, e202209458.

43 V. A. Streltsov, R. S. Ekanayake, S. C. Drew, C. T. Chantler and S. P. Best, Structural insight into redox dynamics of

copper bound N-truncated amyloid-β peptides from in situ X-ray absorption spectroscopy, *Inorg. Chem.*, 2018, **57**, 11422–11435.

44 A. Gaur, W. Klysubun, N. N. Nair, B. Shrivastava, J. Prasad and K. Srivastava, XAFS study of copper (II) complexes with square planar and square pyramidal coordination geometries, *J. Mol. Struct.*, 2016, **1118**, 212–218.

45 V. L. Sushkevich, O. V. Safonova, D. Palagin, M. A. Newton and J. A. van Bokhoven, Structure of copper sites in zeolites examined by Fourier and wavelet transform analysis of EXAFS, *Chem. Sci.*, 2020, **11**, 5299–5312.

46 W. Kosaka, N. Eguchi, T. Kitayama, R. Sato, R. Nakao, Y. Sekine, S. Hayami, K. Taniguchi and H. Miyasaka, Impact of layer stacking manner on the lithium-ion-battery performance in electrically neutral tetraoxolene-bridged iron (II) hexagonal layer metal-organic frameworks, *Chem. Mater.*, 2024, **36**, 3563–3573.

47 Y. Wu, Z. Jiang, Z. Lin, Y. Liang and H. Wang, Direct electrosynthesis of methylamine from carbon dioxide and nitrate, *Nat. Sustain.*, 2021, **4**, 725–730.

48 L. Zhou, X. Chen, S. Zhu, K. You, Z. J. Wang, R. Fan, J. Li, Y. Yuan, X. Wang and J. Wang, Two-dimensional Cu plates with steady fluid fields for high-rate nitrate electroreduction to ammonia and efficient Zn-nitrate batteries, *Angew. Chem., Int. Ed.*, 2024, **136**, e202401924.

49 L. Xu, T. Liu, D. Liu, A. Xu, S. Wang, H. Huang, X. Liu, M. Sun, Q. Luo and X. Zheng, Boosting electrocatalytic ammonia synthesis via synergistic effect of iron-based single atoms and clusters, *Nano Lett.*, 2024, **24**, 1197–1204.

50 W. Liu, J. Chen, Y. Wei, Y. He, Y. Huang, M. Wei, Y. Yu, N. Yang, W. Zhang, L. Zhang, F. Saleem and F. Huo, Regulating local electron distribution of Cu electrocatalyst via boron doping for boosting rapid absorption and conversion of nitrate to ammonia, *Adv. Funct. Mater.*, 2024, **34**, 2408732.

51 K. Liu, H. Wang, L. Chen, J. Li and F. Dong, Synergistic degradation of NO and C_7H_8 for inhibition of O_3 generation, *Appl. Catal., B*, 2022, **312**, 121423.

52 Z. Gu, Y. Zhang, X. Wei, Z. Duan, Q. Gong and K. Luo, Intermediates regulation via electron-deficient Cu sites for selective nitrate-to-ammonia electroreduction, *Adv. Mater.*, 2023, **35**, 2303107.